Astron. Astrophys. 318, 608–620 (1997)

ASTRONOMY
AND
ASTROPHYSICS

The H_2 structure of OMC–1⋆

H. Schild[1], **S. Miller**[2], **and J. Tennyson**[2]

[1] Institut für Astronomie, ETH-Zentrum, CH-8092 Zürich, Switzerland (hschild@astro.phys.ethz.ch)
[2] Dept. of Physics and Astronomy, University College London, Gower Street, London WC1E 6BT, UK

Received 5 January 1996 / Accepted 2 May 1996

Abstract. We have obtained narrow-band images of the Orion Molecular Cloud OMC–1 in various infrared transitions of molecular hydrogen. The molecular emission from levels with low excitation energies ($\lesssim 15\,000$ K) is made up of numerous linear, jet–like structures. Their collimation factor is typically about 10 and there is no appreciable outward broadening. Most of these structures are arranged radially and seem to originate from an area close to IRc2. They however only become detectable at a projected distance of $\sim 10^{17}$ cm from the IRc2 area. The projected length of the linear features is a few times 10^{17} cm. Some of the H_2 fingers seem to be associated with fast moving H_2O masers.

H_2 emission from higher levels ($\gtrsim 19\,000$ K) shows a different nebular structure: Two nebulosities, one around BN which is bipolar and the other one extending north–eastwards of IRc2 in the Peak 2 region, are detected. Images in various continuum wavelengths show the same pattern as the H_2 emission from high levels.

From these images and in conjunction with long slit K and L band spectra of the Peak 2 region we obtain a map of the molecular temperature in OMC–1. The resulting temperature distribution shows little spatial structure on small or intermediate distance scales. It does not show the jet-like structures anymore but displays radial symmetry.

The highly structured H_2 emission is mainly due to strong density rather than temperature variations. The observations suggest that the H_2 emission in the linear structures comes from a thin sheet with a thickness of less than one hundredth of the jet width. It is most likely due to molecular material swept up or entrained into the jet from the outside.

The visual impression provided by high resolution images is that of very dynamic processes disrupting a molecular cloud. The observed structure has been described by the wakes of dense "bullets" ploughing through the surrounding molecular gas. The smooth and only radially variable temperature distribution can however best be interpreted in terms of instabilities in the interaction zone of a stellar wind which collides with surrounding dense molecular material. A thin layer of shocked material is subject to rapidly growing instabilities which may be responsible for the observed linear structures. We draw attention to the fact that the "thin layer instability" in rapidly cooling radiative shock zones may be more important than Rayleigh-Taylor instabilities.

We have also obtained Fabry–Pérot images of OMC–1 in the light of selected K band transitions of the molecular ion H_3^+. These include $2\nu_2^2$ R(6) at 2.0933 μm, $2\nu_2^2$ Q(4) at 2.1944 μm, $2\nu_2^2$ R(8) at 2.1342 μm, $2\nu_2^2$ P(5) at 2.2028 μm and $2\nu_2^2$ P(3) at 2.2039 μm. No H_3^+ was detected. We also observed Peak 2 spectroscopically in the L band but again without a detection of H_3^+. These observations set a probable upper limit of the H_3^+ concentration of 8.5×10^9 cm^{-2} in OMC–1.

Key words: ISM: Orion molecular cloud – ISM: molecules – jets and outflows – instabilities – infrared: ISM: lines

1. Introduction

The first detection of infrared quadrupole emission of H_2 in any astronomical object was the 1976 observation by Gautier et al. (1976) of what is now known as OMC–1. The H_2 emission covers an area of several square arcminutes and is located in the giant Orion Molecular Cloud, at a distance of about 450 pc. It contains the much-studied Becklin-Neugebauer object and the Kleinmann-Low nebula, as well as a number of compact infrared emission sources. According to the review by Genzel & Stutzki (1989), BN-KL is a very dense, clumpy molecular core in which most of the radiation emanates from a few major luminosity sources, of which BN itself and IRc2 - located about 10″ south–east of BN - are the most important.

For more than a decade the standard H_2 map of OMC–1 was that obtained by Beckwith et al. (1978), using the 1-0 S(1) line. Constructed at an angular resolution of 5″, this showed OMC–1 to have two extended lobes and a number of emission peaks. But, overall, the spatial distribution of H_2 emission was fairly smooth. Recent, higher resolution, images of OMC–1 (Lane 1989; Allen & Burton 1993; Schild et al. 1995), however, show

Send offprint requests to: H. Schild

⋆ Based on observations obtained at the European Southern Observatory, La Silla, Chile and the United Kingdom infrared Telescope on Mauna Kea, Hawaii

it to be a highly dynamic region, with a number of fingers or jets seemingly driven by the central luminous sources referred to by Genzel & Stutzki (1989). Some of the most northern extensions of the fingers described by Allen & Burton have also been identified in HST narrow band images (e.g. O'Dell 1995). They have the appearance of Herbig Haro objects and are referred to as HH 205, HH 206 and HH 207. Their optical detection indicates that they are not deeply embedded in the molecular cloud anymore.

BN is considered to be a young star of mass 15 $M_\odot$ and IRc2 a similar object, somewhat more massive at 25 $M_\odot$. More or less strongly collimated outflows from such young stars appear to be common, producing Herbig Haro objects where they collide with dense surrounding gas. In their analysis of images from the north–west quadrant of OMC–1, Allen & Burton (1993) consider compact knots of material – or "bullets" as Mac Low (1995) terms them – to have been ejected either from BN or IRc2, traveling up to 2×10^{17} cm in less than 1000 years. More recently, Stone et al. (1995) have attempted to model the observed structure in terms of Rayleigh-Taylor instabilities produced by the radially symmetric collision of an old, slow stellar wind with a more rapidly propagating young wind. The possibility of such fragmentation because of shell instabilities has already been known for some years (e.g. Rożyczka & Tenorio-Tagle 1985)

In this paper, we present images of OMC–1 taken in a number of wavelengths sensitive to ro-vibrational transitions of H_2, whose upper energy levels correspond to temperatures ranging from 6500 K (1-0 S(0)) to 39 000 K (8-6 O(5)). These show up various structures in the cloud from the full jet-like distribution of intensity seen in the 1-0 S(1) image to diffuse nebulosity surrounding BN and the region known as Peak 2. We attempt to analyse the structures shown using wavelet analysis. We make use of spectroscopy to determine the temperature profile of Peak 2 and ratio images to produce temperature and column density maps of the region. Wavelet analysis is used to help determine whether temperature or density variations are responsible for the main structures observed in the images.

Another motivation for the work presented here was to see if it were possible to detect emission from H_3^+ in OMC–1. This fundamental molecular ion has long been known to be an important constituent of the interstellar medium (e.g. Dalgarno 1994). However despite a number of documented attempts to observe H_3^+ spectra (Oka 1981; Geballe & Oka 1989; Black et al. 1990), it has so far defied detection. All these attempted detections tried to observe cold ($T < 50$ K) H_3^+ absorption against suitable star light in the L window. Black et al (1990) gave an upper limit of the H_3^+ column density of $\sim 5 \times 10^{15}$ cm^{-2} towards the highly obscured sources NGC 2264 IRS and AFGL 2591. This limit is close to that predicted by theoretical models. Geballe & Oka (1989) produced an upper limit of 3 - 4 $\times 10^{14}$ cm^{-2} in front of BN.

Successful detections of H_3^+ emission in the giant planets (Drossart et al. 1989; Trafton et al. 1993; Geballe et al. 1993) and elsewhere (Miller et al. 1992) have been made in the L and K windows. In the observations reported here we attempted to observe similar H_3^+ emissions in a similarly active region. The H_2 emissions from OMC–1 suggest that it is hot enough to produce H_3^+ emissions. However our observations detected no H_3^+. Instead, we can only present upper limits to the H_3^+ column density, although these are more sensitive to the assumed temperature of the column than those obtained from attempted detections of cold H_3^+ via absorption.

2. Observations

2.1. ESO

We obtained a series of infrared images of OMC–1 during two observing runs from Dec 29, 1993 to Jan 1, 1994 and Dec 24 to 27, 1994 with the ESO/MPI 2.2m Telescope and the infrared camera IRAC2.

A Fabry–Pérot filter was centered at various K band transitions of the H_2 molecule and the H_3^+ molecular ion. The bandwidth of the FP was 1.9 nm and the accuracy of the wavelength setting was 0.5 nm. The detector was a 256×256 NICMOS array with a field of view of about $2'$. The detector pixel projected to $0.51''$. Integration times were 5 min on source and 5 min on two separate background positions. For weaker lines, several cycles were averaged. The seeing conditions during the first observing run were excellent and the measured FWHM of the stellar images was $0.8''$. The second run had slightly worse seeing conditions and in addition suffered from an RA tracking problem. Some of the images are thus slightly elongated in the east–west direction.

The H_2 transitions observed were S(0) 1–0, S(1) 1–0, S(1) 2–1, S(2) 2–1, S(3) 2–1, S(3) 3–2, S(3) 4–3, Q(1) 1–0 and O(5) 8–6. The S(1) 2–1 at 2.2477 μm image is contaminated by emission from M42. Possibly this leakage is due to [Fe III] radiation. An image of OMC–1 taken at 2.122 μm is shown in Fig. 1 and a continuum subtracted and deconvolved image in Fig. 2. Continuum images were obtained at 2.1319 μm, 2.1577 μm, 2.2098 μm, 2.2334 μm and 2.3652 μm. The continuum was found to be constant within the observational errors and the frames with the best seeing images were averaged. Image deconvolution (Fig. 2) was achieved with the Lucy algorithm (Lucy 1974) after 20 iterations and a bright star in the field as PSF.

The transitions used for the search for the molecular ion H_3^+ were those in the $2\nu_2^2$ overtone band used by Drossart et al. (1989) in their original detection of H_3^+ on Jupiter. Specifically we used R(6) at 2.0933 μm, Q(4) at 2.1944 μm, R(8) at 2.1342 μm, P(5) at 2.2028 μm and P(3) at 2.2039 μm. Continuum images were taken at 2.0948 μm, 2.1330 μm, 2.1370 μm, 2.1924 μm, 2.1934 μm, 2.1954 μm, 2.1964 μm, 2.2052 μm.

Since that Fabry–Pérot filter is uncooled, there are strong thermal emission rings. Although these can be subtracted with proper sky frames, detection of weak emission towards the detector edge is hampered. Pairs of flatfield frames were taken from a dome screen with the lamp on and off such that the thermal FP emission could also be removed in the flatfields. The Fabry–Pérot images were flux calibrated with stars taken from McCaughrean and Stauffer (1994). Typically we have about a dozen stars in the southern third of our frames in common. The

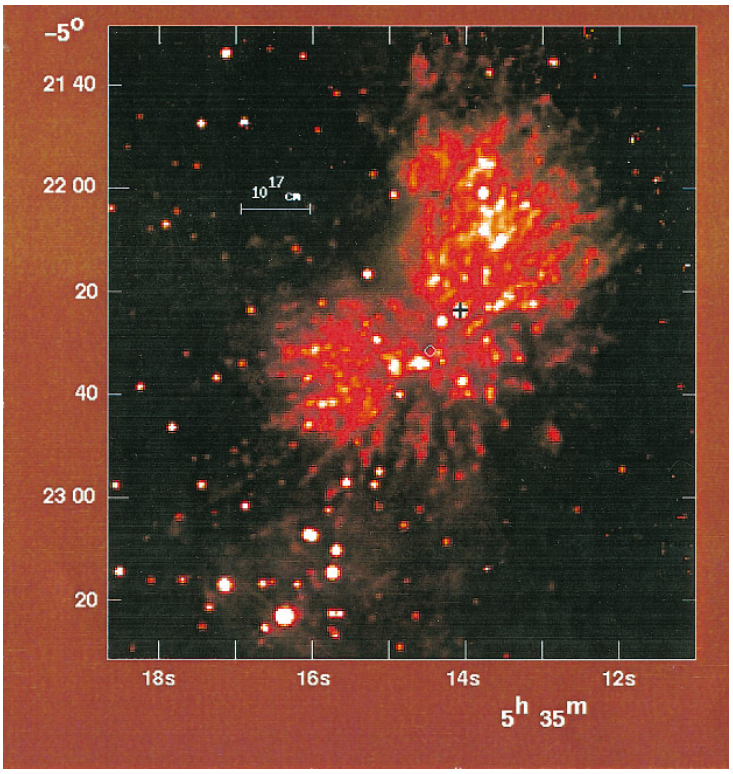

Fig. 1. Inner region of OMC–1 at a wavelength of 2.121 μm. The Becklin–Neugebauer object is marked with a black cross. The white circle shows the position of the compact radio source I which lies close to IRc2 (Menten & Reid 1995). The Trapezium stars are visible at the bottom. Coordinates are for J2000.0.

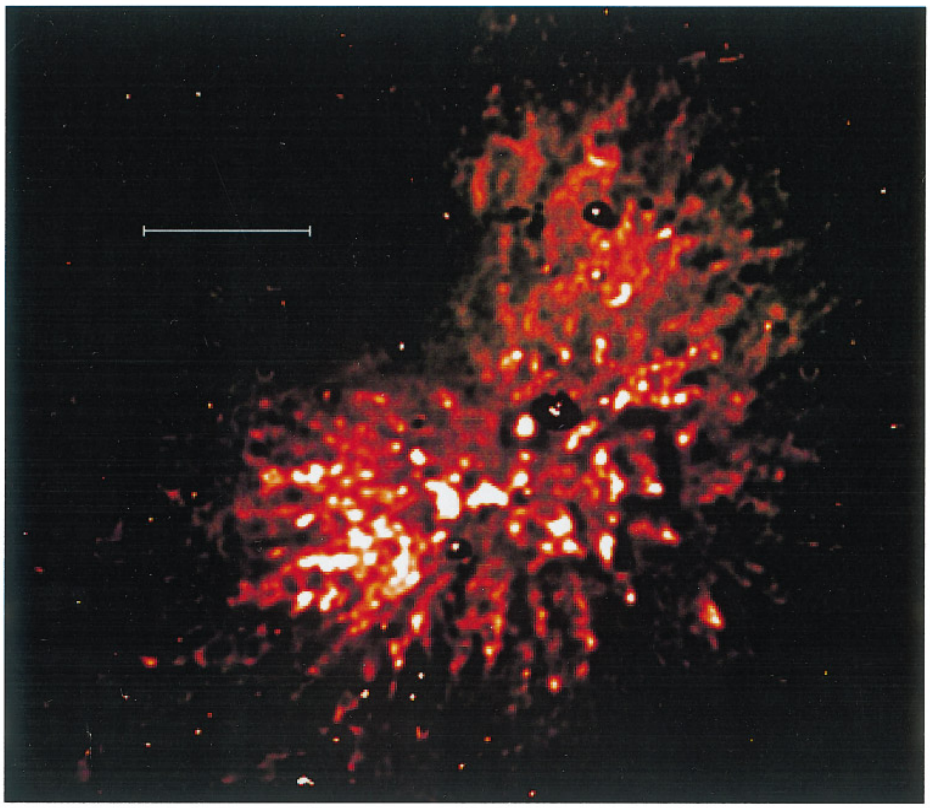

Fig. 2. Continuum subtracted and deconvolved version of the above image. The horizontal bar represents 20″.

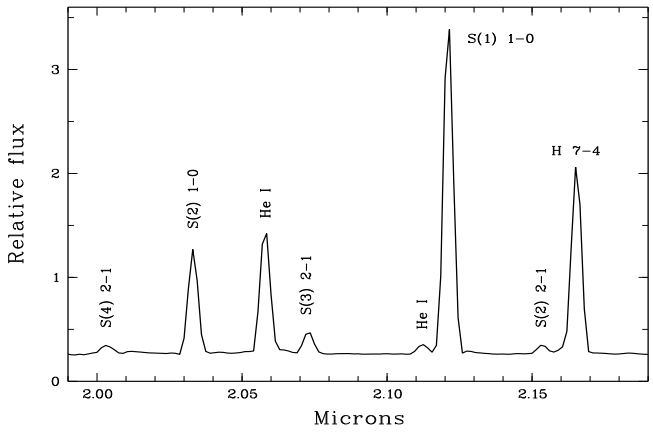

Fig. 3. K band spectrum taken at the brightest knot of Peak 2 (see Fig. 6). Transitions of molecular hydrogen are marked with their spectroscopic designation. The lines of hydrogen and helium are dominated by emission from M42. The observational errors are comparable to the line thickness.

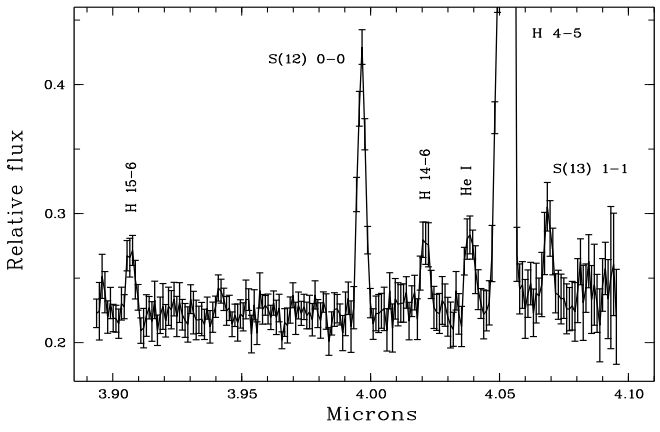

Fig. 4. High resolution spectrum around 4 μm of the brightest knot in the Peak 2 area (see Fig. 6). The lines of molecular hydrogen (S) and atomic species are indicated.

RMS scattering of the local sensitivities thus obtained at the position of each calibration star was less than 10 %. We estimate that the accuracy of the absolute intensity calibration across the area of OMC–1 is better than 50 % and that on small scales ($\lesssim$ 20″) it is better than 20 %.

2.2. UKIRT

We observed the Peak 2 region in OMC–1 spectroscopically during the nights from Sep 29 to Oct,1 1993 with the UK infrared Telescope and the facility spectrometer CGS4. The detector was an InSb array with 58 × 62 pixels. A K band spectrum was obtained with the 75 lines/mm grating and the 300 mm camera. It covered the wavelength range from 1.99 to 2.20 μm with a resolution of R ≈ 1400. The slit length was 90″ and a pixel projected to 1.5″ × 1.5″ on the sky. Exposure times were 150 sec, both on sky and target. A relative flux calibration was obtained with observations of the B8 star BS 1713.

With the Echelle grating and the same camera a spectrum centered at 4.0 μm was obtained. This configuration provides a nominal dispersion of 19 km/sec per pixel. The resolution measured from the argon arc is R ≈ 9000. Because of anamorphic magnification in this configuration the pixel projects to 1.9″ × 1.2″, in the spatial and spectral directions, respectively. Sky background exposures were taken at offsets of 2′. Total integration times on the sky and target were 300 sec each. For flux calibration the standard star BS 788 was observed. The slit was orientated east–west for both observations and its position on OMC–1 is shown in Fig. 6.

A further spectrum at the same sky position was obtained during the night of Jan 29, 1994 as a service observation by Tom Geballe and John Davies. The 150 l/mm grating together with the short (150 mm) camera provided a wavelength coverage from 3.9 to 4.1 μm with a resolution of R ≈ 1200. The same detector was used but with this camera the pixel size corresponds to 3″ on the sky. The total exposure time was 84 sec on target and sky each.

As an illustration we show the observed spectra at the strongest emission peak in Figs. 3 & 4. In the K window (Fig. 3) lines of molecular hydrogen dominate the spectrum. There are also recombination lines of hydrogen and helium from the Orion Nebula M 42. These lines have a completely different spatial profile such that in the case of both, strong and weak lines, a clear separation between molecular (OMC–1) and atomic (M 42) origin is possible.

In the spectrum around 4 μm (Fig. 4) the S(12) 0–0 and S(13) 1–1 transitions of molecular hydrogen are clearly detected. The strongest emission line is Brα. We note a weak unidentified emission feature at 3.942 μm.

Our Echelle spectrum also covers the S(12) 0-0 line which has its upper level at 15 549 K. Over most of the length of the slit the line is unresolved, i.e. the intrinsic line width is less than 33 km/sec. At the western edge of the bright spot (cf. Fig. 6), the intrinsic line width suddenly increases to about 60 km/sec. Within a separation of only 2″, the turbulent velocity of the molecular hydrogen can therefore increase by a factor $\gtrsim$ 2.

Our spectral observations cover the wavelengths of several transitions of the molecular ion H_3^+. In the K band we cover the $2\nu_2^2$ transitions R(6) at 2.0933 μm and R(8) at 2.1342 μm. In the range 3.9 – 4.1 μm there is a blend of two ν_2 Q(3) transitions at 3.987 μm and the ν_2 Q(1) transition at 3.953 μm (Kao et al. 1991). No lines were detected, however. Our spectra may be used to provide upper limits to the H_3^+ concentration, which will be derived and discussed below.

3. H_2 morphology of OMC–1

Fig. 1 shows an observed image of the OMC–1 complex at 2.121 μm. In the north are Beckwith's Peak 5 (which nearly coincides with IRc9) and Peak 1. Near the centre BN shows up brightly. Peak 3 is resolved into two bright sources, south–east of BN. IRc2 lies a few arcseconds north–west of a bright trian-

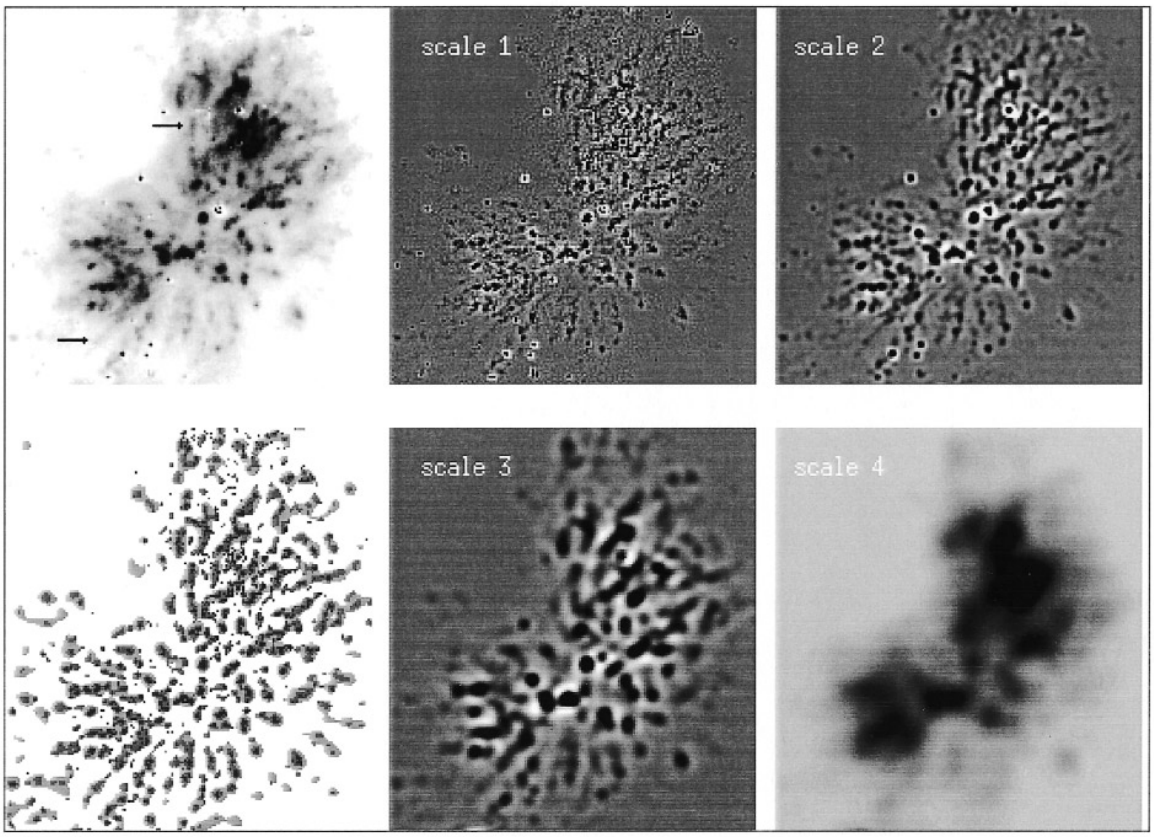

Fig. 5. Wavelet analysis of the H_2 S(1) 1–0 emission in OMC–1. Top left: Original continuum subtracted image. The northern jet and one of the south–eastern jets are marked by the arrows (see text). Bottom left: Wavelet transform with the different scale images superposed. Four panels at right: Wavelet transforms at four different scales to enhance structure at small-scales (top center), intermediate-scales (top right and bottom center) and large-scales (bottom right).

gular shaped emission area. East–south–east of Peak 3, Peak 2 is a bright region which is resolved into a network of crossing linear structures. A strong emission knot can be seen south–east of BN. The central object in Peak 5 appears to be surrounded by a partial ring in the north–east and south–west. In the neighbourhood of Peak 1, linear strings stretch from south–east to north–west.

3.1. Structural analysis

The continuum subtracted image at 2.121 μm (Fig. 5, top left) shows that the S(1) 1–0 emission of molecular hydrogen is mainly due to a superposition of near–linear features. Without wishing to prejudice the discussion below on possible mechanisms for the formation of the structure observed, we will follow Allen & Burton (1993) in calling these "jets". They seem to expand in all directions except the north–eastern quadrant. Between a direction due west and approximately east–south–east, there are perhaps as many as ten distinct jets. There is in particular a long, strong jet going almost due north which is marked by one of the arrows in Fig. 5.

To assist in understanding the morphology of the region, we have applied a wavelet analysis technique. Extensive literature about wavelet transforms and their application to multiresolution analysis exists (Mallat 1989; Chui 1992; Meyer 1992; Ruskai et al. 1992). Here we use it to emphasise the morphological structure seen on a number of distance scales. We have used the à-trous algorithm with linear scaling functions. The resulting wavelet transforms of the S(1) 1–0 image are shown in Fig. 5. Each scale has double the resolution of the previous one. Scale 1 to 4 thus emphasize structure at a typical resolution of $4''$, $2''$, $1''$ and $0.5''$, respectively. Fig. 5 (bottom left) also shows the composite image that we obtain if all transforms are superposed.

At OMC–1, one arcsecond is subtended by a linear distance of 7×10^{15} cm. Fig. 5 thus shows respectively linear structures on a scale of $\lesssim 4\times10^{15}$ cm, 7×10^{15} cm, 1.5×10^{16} cm, and structures larger than 3×10^{16} cm. The jets are best visible at scales 2 and 3. Scale 1 is dominated by small, bright knots which are aligned along the jets. At the largest scale, an image similar to that of Beckwith et al. (1978) is recovered, showing the lobes and emission peaks. In particular, Peak 2 is clearly identified in the south–eastern lobe.

In the wavelet analysis, linear structures show up most clearly in the intermediate scale images, and we take this to be a signature of the jets. They have a typical projected length

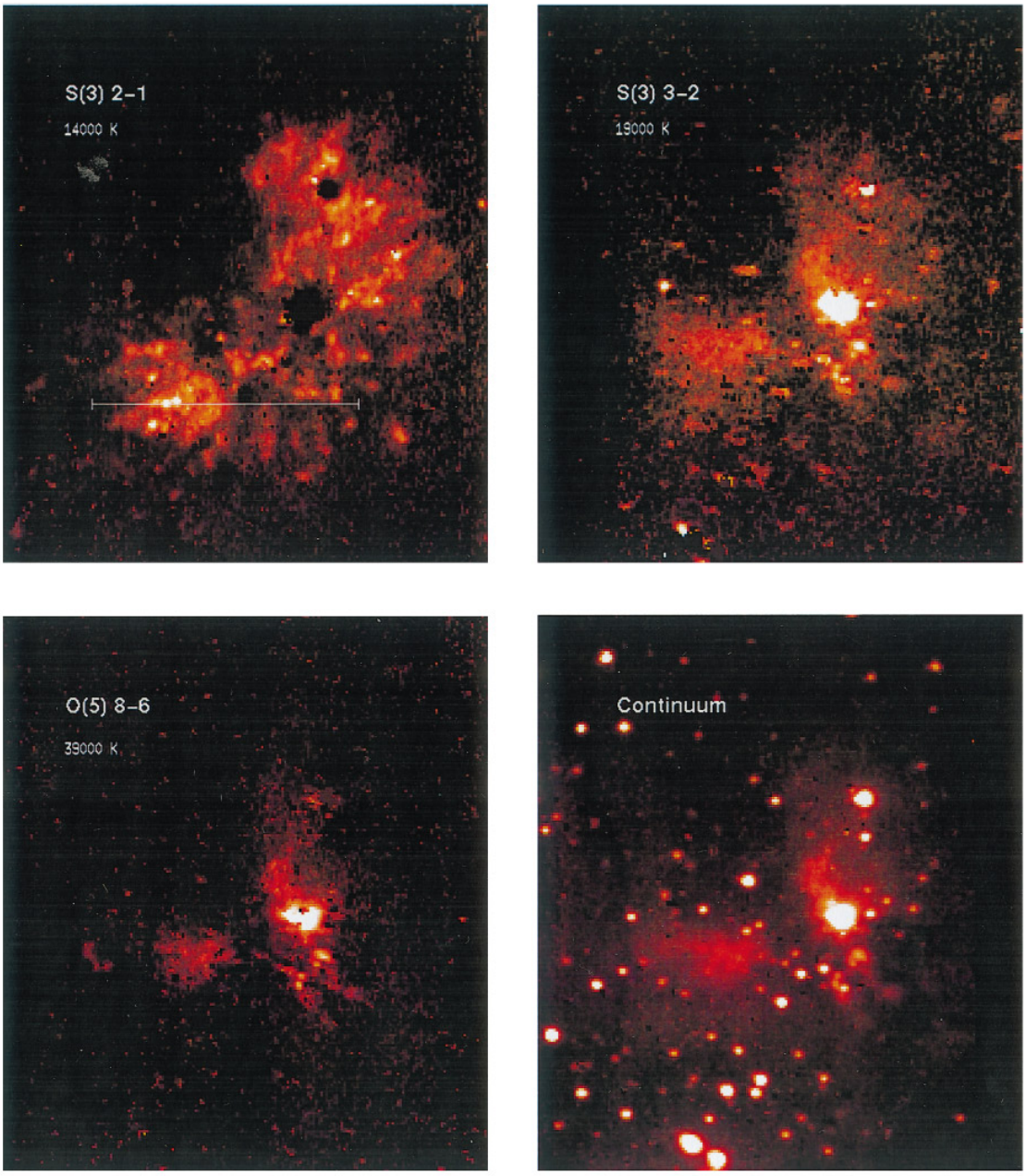

Fig. 6. OMC–1 in the light of the H_2 transitions S(3) 2–1, S(3) 3–2, O(5) 8–6 and the continuum (taken at 2.098 μm and 2.334 μm). The white line in the top left panel shows the position of the slit of our spectroscopic observations. The H_2 images are continuum subtracted.

of 1.5×10^{17} cm; a typical width is 1.3″, which – after correction for the seeing conditions – implies an intrinsic width corresponding to 7×10^{15} cm. The jets appear to be made up of a string of emission knots, sometimes discernibly connected by weaker, linear emission, which shows up both in the intermediate scale image and at the smaller scale (Fig. 5). The blobs are fairly evenly spaced and with a typical separation of 2″. This projects to a few times 10^{16} cm. At the end of many of the jets are bright heads, whose S(1) 1–0 luminosity is typically a few times 10^{-4} $L_\odot$.

We may use Fig. 5 to assist in tracing the jets back towards the centre. Allen & Burton (1993) conjectured that the features they saw could have come from IRc2 or BN; from our image, the latter would appear to be ruled out by the line of the northern jet, although the other jets do not discriminate so clearly. In the north–western quadrant and north of east–south–east it is more difficult to trace individual jets through the cloud.

The northern jet passes through a bright ring of emission and emerges much weaker in intensity. If the jet and ring structures are indeed connected, it would appear as if the jet hit a clump

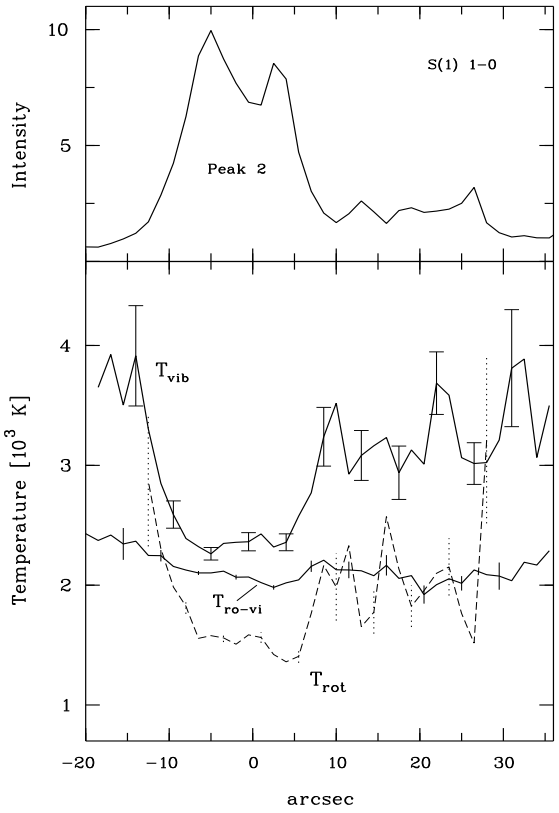

Fig. 7. Molecular temperatures through Peak 2 region. Rotational/vibrational temperature T_{ro-vi}, pure vibrational T_{vib} and rotational T_{rot} (dashed) temperatures along the slit. Only a few representative error bars are plotted. East is to the left. The spatial intensity distribution along the slit of S(1) 1–0 is shown in the top panel. For the slit position and orientation see Fig. 6.

of denser material, causing a radially expanding density wave, while passing through.

The jets do not show any measurable broadening in the outward direction. We have estimated opening angles for two of the jets – the northern one and one in the south–east, marked on Fig. 5 (top left) by taking as jet length only the distance over which they can clearly be traced. This provides as upper limits 13° and 6°, respectively. If IRc2 is taken as source, these values are reduced by about a third. The collimation factor is thus of the order of 10.

3.2. Other H_2 transitions and continuum emission

In Fig. 6 we show OMC–1 in the light of the H_2 transitions S(3) 2–1, S(3) 3–2, O(5) 8–6 and a continuum wavelength. S(3) 2–1 has an excitation temperature of about 14 000 K, i.e. twice as high as S(1) 1–0. The morphology of OMC–1 is nonetheless similar in both lines. Although S(3) 2–1 is considerably weaker, all structures seen in S(1) 1–0 are also present in S(3) 2–1. The situation changes drastically if we turn to the transitions which originate from higher levels. S(3) 3–2 and O(5) 8–6 with excitation temperatures of about 19 000 K and 39 000 K respectively do not show any of the numerous linear structures visible at the lower temperatures. There only remain two larger nebulosities, one around the BN object and one stretching to the north–east of IRc2. The nebulosity near BN seems to have a bipolar structure. Apparently, there are thus two different regimes of H_2 emission, a cool one which displays the pattern of numerous linear features and a weaker hot and more compact one which presumably is excited under more extreme shock conditions.

We also have obtained a series of continuum images at various wavelengths. We do not find any significant changes at different wavelengths, so in Fig. 6 we show the sum of the images taken at 2.098 and 2.334 μm. There are a number of stellar sources, many of which have already been catalogued (Lonsdale et al. 1982; McCaughrean & Stauffer 1994). There is weak nebular continuum emission which is most likely due to hydrogen recombination radiation or dust emission. The similarity of the continuum image with the H_2 O(5) 8–6 may indicate that hot molecular hydrogen either is located close to the ionisation front or even coexists in protected pockets with ionised hydrogen.

4. Physical conditions

In this section we determine the structure of the temperature and the column density of H_2 in OMC–1. In particular, we address the question of whether intensity variations in the S(1) 1–0 emission are due to temperature or density fluctuations. We also examine in more detail the H_2 emission conditions in the North-jet and address the question of how thick the emitting layer is.

4.1. Molecular temperature

Our observations provide two different means to measure the temperature of molecular hydrogen. We firstly have spectra in the range 1.99 to 2.20 μm through a long slit covering the eastern and southern part of OMC–1. We secondly also have the Fabry–Pérot images in a number of H_2 transitions which cover the other parts of OMC–1.

4.1.1. K band spectrum of Peak 2

For our spectroscopic observations the slit was positioned onto the bright region of Peak 2 and passed south of Peak 3 (cf. Fig. 6, top left). Besides S(1) 1-0 (2.121 μm), the spectrum shows the H_2 transitions S(4) 2-1 (2.003 μm), S(2) 1-0 (2.033 μm), S(3) 2-1 (2.072 μm) and S(2) 2-1 (2.154 μm). We have sufficient signal in these lines and can use various ratios to determine both, rotational and vibrational temperatures. A vibrational temperature T_{vib} is provided by S(2) 1-0 and S(2) 2-1 and a rotational temperature T_{rot} via S(2) 1-0 and S(1) 1-0. In the latter case, the energies of the upper levels are relatively close which leads to larger errors in the temperature measurement. The best combination in terms of line strength and energy difference can be obtained with the S(3) 2–1/S(1) 1–0 ratio which we denote T_{ro-vi} (Fig. 7). The observational errors are dominated by the uncer-

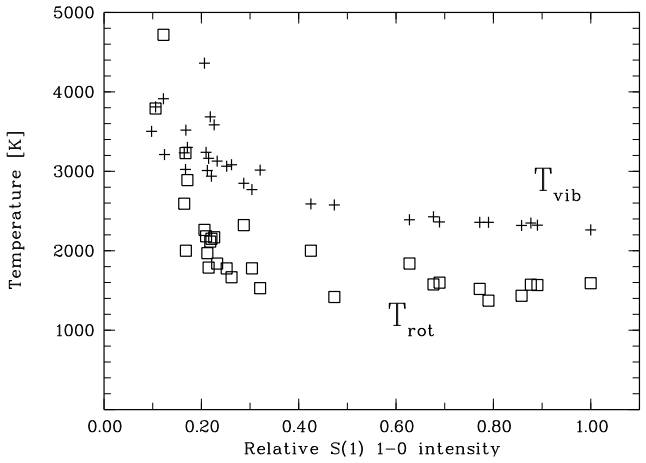

Fig. 8. Rotational (squares) and vibrational (crosses) temperature versus the relative intensity of the H_2 S(1) 1-0 line.

tainties involved with the continuum subtraction particularly in the outskirts of the nebulosity where the fluxes are low.

The ro-vibrational temperature we measure is remarkably constant at about 2000 K over most of the nebulosity except at the edges where it increases slightly by a few hundred K. The vibrational temperature is systematically higher, between 2500 K and 4000 K and shows a steeper increase at the edges. The broad depression in T_{vib} and T_{rot} between +5″ and –10″, occurs in the most luminous region of the Peak 2 area. The rotational temperature T_{rot} is systematically lower than T_{vib} but consistent with T_{ro-vi} outside of the Peak 2 area.

The maxima in T_{vib} to the west of Peak 2 tend to coincide with low emission regions which occur between different jet–like features. These variations are however barely significant and might be mimicked by variable extinction. We have not applied any reddening corrections to the intensity ratios because the extinction is likely to be rather patchy. An increase of the line ratio S(2) 1–0/ S(2) 2–1 by 30% in the inter-jet regions would remove the structure in T_{vib}. This would correspond to a local increase of the dust absorption by ~ 0.25 mag. Such reddening variations have been measured by Scoville et al. (1982) who also concluded that in some parts of OMC–1, the H_2 emission is anti–correlated with the extinction. It is therefore likely that most of the structure in T_{vib} can be attributed to variable extinction.

The difference between T_{vib} and T_{rot} in the Peak 2 area can not be due to extinction because the wavelength separation of the respective transitions are similar. T_{ro-vi} on the other hand is very little affected by extinction because the transitions are only separated by 0.05 μm in wavelength and we therefore believe that this ratio provides the best temperature estimator. A possible explanation for the difference between T_{rot} and T_{vib} at high S(1) fluxes is that regions of strong S(1) 1-0 emission correspond to locations where the gas densities are such as to effect rotational thermalisation, whereas the excited vibrational levels remain slightly overpopulated as a result of shock heating. At the lowest gas densities, overpopulation of both higher rotational and excited vibrational levels is more pronounced, since gas densities are insufficient to thermalise either.

Fig. 8 summarizes the behaviour of T_{rot} and T_{vib} as a function of the intensity of the S(1) 1-0 line. The low temperatures occur where the S(1) line is strong whereas, at locations where it is weak, the temperature seems markedly increased. In regions with moderate to strong S(1) 1-0 emission the temperature is rather constant with $T_{rot} \approx 1600$ K and $T_{vib} \approx 2300$ K. At low emission levels, both T_{rot} and T_{vib} converge to a hotter temperature around 4000 K. As outlined above, this upturn is at least partly due to variable extinction whereas the difference between T_{rot} and T_{vib} at high S(1) 1–0 intensity levels is attributable to incomplete thermalisation.

4.1.2. Fabry–Pérot images

We can use our Fabry–Pérot images to obtain further spatial information about the H_2 temperature distribution. Best suited are the transitions for which emission was detected over as large parts of the object as possible. This leaves the S(3) 2–1, S(1) 1–0 and S(0) 1–0 transitions. Because of still appreciable extinction even in the K band, we selected the S(3)/S(1) ratio because the respective transitions have similar wavelengths. The resulting temperature corresponds to T_{ro-vi} of the previous section. We note that the use of the S(3)/S(0) ratio would lead to a qualitatively similar temperature structure, although the error bars would be larger.

In this section we mainly focus on the morphological structure of the molecular temperature rather than numerical values. In Fig. 9 we display the H_2 temperature distribution of OMC–1 as obtained from the S(3)/S(1) ratio together with its wavelet transform at three different scales. The wavelet scales are the same as those described in Sect. 3.1 (Fig. 5).

The most striking feature in Fig. 9 is, that the H_2 temperature is rather uniform across the face of the object. The scale 4 wavelet transform shows that there is a large scale radial gradient in the sense that the outer rim is slightly hotter than the central part. The lowest temperatures of around 1700 K occur in the innermost regions around Peak 1. The temperature also increases westwards to up to about 2400 K and south–eastwards to 2800 K, which is, within the expected error bars, consistent with the spectroscopic results of the previous section. The wavelet scales 2 and 3 do only show very little or no structure at all. The bright spots in both scales are due to amplified image artifacts or represent areas where the temperature is not defined because of too low flux levels of S(3) 2–1.

In conclusion, we find that in OMC–1 the temperature structure shows only variation at the scale of a few arcseconds and that in particular, the linear jet–like features are not due to local temperature enhancements.

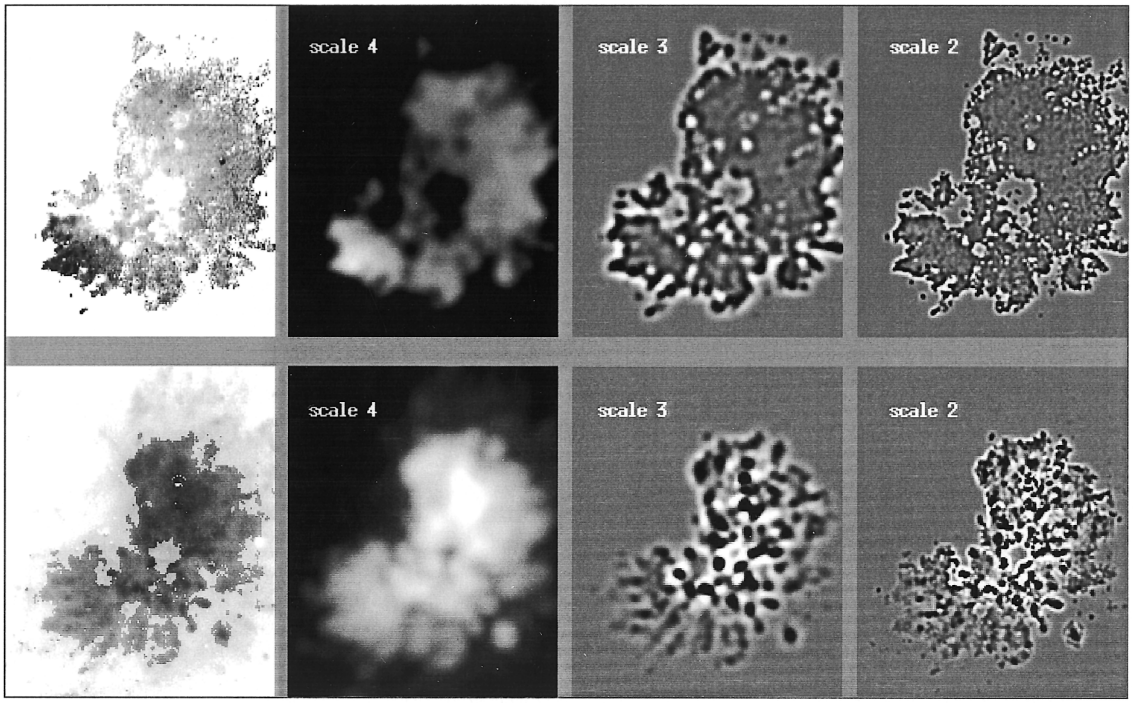

Fig. 9. Morphological structure of the H_2 temperature and column density in OMC–1. Upper row: T_{ro-vi} map (left) and its structure at various scales from wavelet analysis. Lower row: Same for column density. Note that the dominant structure in the temperature occurs at scale 4 while for the column density it occurs at scales 2 and 3.

4.2. H_2 column density

The column density of molecular hydrogen $N(H_2)$ can be obtained from:

$$N(H_2) = \frac{4\pi\ I_{ij}\ Z(T)}{h\nu_{ij}\ A_{ij}\ g_i\ e^{E_i/kT}} \quad (1)$$

where $Z(T)$ is the partition function of H_2 and I_{ij}, A_{ij} and ν_{ij} are the observed intensity, transition probability and frequency of the transition in question. E_i stands for the energy and g_i the statistical weight of the upper level. The partition function Z was taken from Irwin (1987).

The resulting column density distribution across OMC–1 was deduced with the continuum subtracted image of S(1) 1–0 and the temperature distribution from the previous section. We have not applied any extinction correction because we are interested in the morphological structure of the column density rather than numerical values. At large scales the column density retains its blobby character whereas at scales 2 and 3 the linear jet–like features are apparent again although they are less conspicuous than in the direct images (Fig. 9). Clearly, there is a striking difference in the morphological structure of the H_2 column density and molecular temperature at all scales.

4.3. Physical conditions in the North-jet

In Fig. 10 we show cuts from the above intensity, temperature, and column density images along the North-jet (marked in Fig. 5). The horizontal axis is given in arcseconds and starts at the bright knot north–east of the BN object. The "blob" structure mentioned above shows up clearly as a series of fairly evenly spaced peaks in the intensity. This pattern is followed closely by the density. But the temperature – with the exception of a small peak some $10''$ from the origin (which may be an artifact) – increases slowly and fairly evenly towards the northern edge of OMC–1. Assuming that the thickness of the emitting region is similar to the jet width, a typical column would by 7×10^{15} cm and with an observed column density of a few times 10^{18} molecules per cm^2, the average density of molecular hydrogen becomes only about 500 cm^{-3}. This assumes that the jet is homogeneously filled with hydrogen molecules. If, on the other hand, the level population is thermalised, a H_2 density of at least 10^6 cm^{-3} is required. In this case only a thin layer of molecular hydrogen can account for the observed emission. In that situation the H_2 emitting surface is only a thin sheet with a thickness of less than 10^{12} cm which corresponds to $\lesssim 0.05\,\%$ of the jet cross section. It is thus conceivable that the molecular hydrogen is entrained from the surrounding molecular cloud into the jet and is rapidly destroyed as it is sucked inwards.

This argument, that the H_2 emission is generated in an extremely thin layer, rests on the assumption that the Boltzmann level population of molecular hydrogen is maintained by H_2 – H_2 collisions, the efficiency of which then requires $n(H_2) \gtrsim 10^6$ cm^{-3}. New calculations of Mandy & Martin (1993) indicate however that neutral hydrogen may be a more efficient collision partner. For the (1,3) level the critical density lies around 6

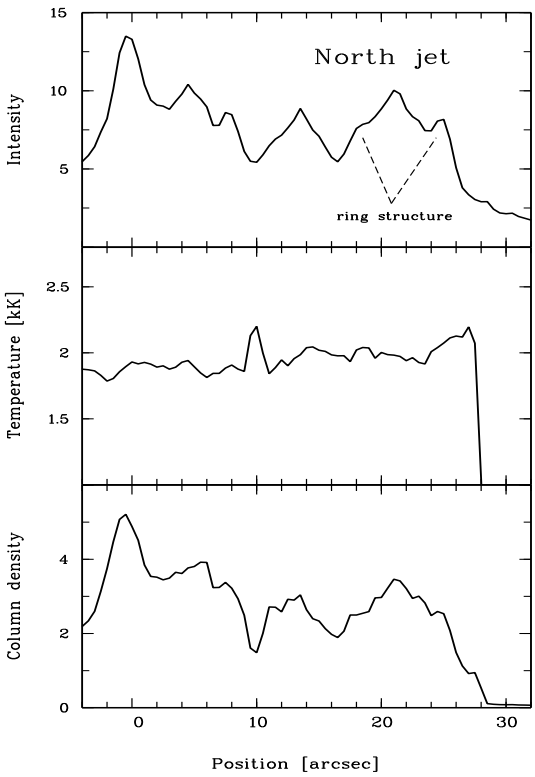

Fig. 10. Physical conditions in the jet heading north (marked in Fig. 6). Top panel: Intensity profile of the H_2 S(1) 1–0 line integrated across the width of the jet in units of 10^{-14} ergs cm^{-2} s^{-1}. Center: Molecular temperature from the S(3) 2–1/S(1) 1–0 line ratio. Bottom: Column density of H_2 in units of 10^{18} molecules per cm^2.

$\times$ 10^3 cm^{-3} at a temperature of 2000 K and if the density of neutral hydrogen is n(H) $\approx$ 0.1 n(H_2), the molecular hydrogen can already be thermalised at densities $n(H_2) \approx 5 \times 10^4$ cm^{-3}. However, even in such a situation, the H_2 emitting material in the North-jet could still not originate from the full width of the jet. It would come from a thicker layer as above but it still would have a width of only about 1 % of the total jet cross section.

5. Upper limits to H_3^+

One of the original aims of our observations was to see if H_3^+ could be detected in the regions of OMC–1 which show strong molecular hydrogen emission. In such regions Neufield & Dalgarno (1989) have argued that concentrations of H_3^+ might reach as high as $10^{-7} \times n(H_2)$, (the density of H_2). Values of the ro-vibrational Einstein A_{ij} coefficients for H_3^+ are typically of the order of 10^2 s^{-1}, some nine orders of magnitude larger than those for H_2. This suggests that, were conditions of thermal equilibrium to pertain, H_3^+ ought to be observable.

Molecular hydrogen can exist in thermal equilibrium at densities of 10^6 cm^{-3}, densities reached easily in shocked interstellar gas. For H_3^+ such densities are sufficient for rotational states within a vibrational sub-level to be thermalised. However, the large ro-vibrational A_{ij} values of H_3^+ mean that gas densities around 10^{12} cm^{-3} are required to reach full ro-vibrational thermal equilibrium. These densities are typical of the atmosphere of Jupiter, but are reachable only in very localised regions - around masers, for example - in the interstellar medium.

In the K window, at temperatures above 1000 K, the strongest emission line is $2\nu_2$R(6), occurring at 2.0933 μm. Our non-detection of this line sets an upper limit of a flux of 5×10^{-16} erg s^{-1} cm^{-2} from the area subtended at OMC–1 by our pixels. This in turn translates into an upper limit on the column density of 4.8×10^8 cm^{-2} in the v=2 vibrational level, if we assume zero extinction. Our non-detection of lines belonging to ν_2 in the L window sets an upper limit of 2.8×10^9 in the v=1 level. Under conditions of complete thermal equilibrium, this translates - at temperatures in the range of 2000 to 3000 K - to an upper limit on the column density $N(H_3^+)$ of $8.5(-0.6, +1.2) \times 10^9$ cm^{-2}. At the lower temperature of 1000 K, our results produce a total H_3^+ column density of no more than 1.3×10^{11} cm^{-2}.

Under non-thermal conditions, the population of H_3^+ in the excited vibrational levels is controlled by collisions with the dominant species, H_2. No measurements of the cross section, $< \sigma v >$, for this process have been made. Values of 10^{-16} to 10^{-15} cm^{3}s^{-1} are usually quoted for H_2/H_2 collisional excitation. But vibrationally excited H_3^+ may additionally be produced by proton-hopping to vibrationally excited H_2. This reaction is expected to occur at close to the Langevin rate for ion molecule reactions, of the order of 10^{-9} cm^{3}s^{-1}. At 2500 K, a median temperature for the entire cloud about 5 % of H_2 molecules are in the vibrationally excited, v=1, state. Proton hopping is thus probably the dominant mechanism for vibrationally exciting H_3^+. We can now make use of a simplified equation of balance for ratio between ground state and vibrationally excited H_3^+, thus:

$$n_i \times A_{ij} = n_j \times < \sigma v > \times n_{H_2} \times f(v = 1) \quad (2)$$

where i corresponds to H_3^+ in a vibrationally excited level, j to H_3^+ in the ground state, and $f(v = 1)$ is that fraction of hydrogen molecules excited to the v=1 vibrational level.

In order to evaluate this equation, we must first assume that the excited H_2 and any emitting H_3^+ are spatially co-existent. We can then use the values obtained for the column densities of H_2 and the upper limit on H_3^+ in the v=2 level in place of $n(H_2)$ and n_i respectively. Together with the value of A_{ij} for v=2$\rightarrow$0 given by Dinelli et al. (1992), this gives an upper limit for the density of H_3^+ in the ground state (which is close to the total H_3^+ concentration under non-thermal conditions) of $n(H_3^+)$ = 40 cm^{-3}. This number is clearly highly dependent on the value chosen for $< \sigma v >$. But the upper limit we set would certainly not rule out relative concentrations as high as 10^{-7} if total densities of 10^8 cm^{-3} were reached locally.

6. Discussion and conclusions

We have obtained Fabry–Pérot images of the OMC–1 star forming region in various K band transitions of the H_2 molecule. These images show a network of narrow linear structures, reminiscent of jets with very small opening angles. From Figs. 9 &

10 it is clear that these jet structures cannot be explained as a result of temperature variations but are due to density fluctuations. This conclusion is reinforced by the wavelet analysis of the temperature map which shows very little structure at small or intermediate scales. Instead the temperature makes only a large scale contribution to the structure of the region. The column density map, on the other hand, shows structure on all of the scales we have used.

From the observed column density and the fact that H_2 needs to be thermalised, we deduce that the H_2 emission comes from a thin sheet only. This argument has already been presented earlier (e.g. Ridgway 1983) but with the higher resolution images now available, the thin sheet is not anymore uniformly covering the lobes of Beckwith et al. (1978) but rather consists of a network of long tubes which are wrapped in a layer of shock excited molecular hydrogen. This molecular material was probably entrained into the path of the passing shocked material which in itself is not visible on H_2 images. The molecular gas is heated to a temperature of up to ~ 3000 K. The fact that we observe this upper limit of the H_2 temperature is due to the strong increase in the collision-induced dissociation coefficient in this temperature range (Roberge & Dalgarno 1982).

6.1. Structure formation mechanisms

The question arises of how the numerous linear structures have been formed. Two types of formation mechanisms can be envisaged: one is jet-driven and the other wind driven. The former process invokes bullets of material which are ejected in various directions (Allen & Burton 1993) and the latter produces the observed linear structures with instabilities in the wind–molecular cloud interaction zone (e.g. Stone et al. 1995).

6.1.1. The jet scenario

In the jet scenario, OMC–1 is a superposition of jets as they are observed in Herbig-Haro objects. A cluster of young stars or pulsed ejection from a single strongly precessing source could in principle produce the observed wealth of linear structures. Regular chains of knots have been detected in many outflows (e.g. in HH 7–11 see Mundt 1985, Bachiller & Cernicharo 1990 or in IRAS 3282 see Bachiller et al. 1991) which indeed have been interpreted as due to a pulsed matter ejection (e.g. Bachiller et al. 1990, Guilloteau et al. 1992). On the other hand, such a knotty structure could also be the consequence of hydrodynamical instabilities in a jet.

If IRc2 is indeed the central object driving the dozens of radially expanding jets, then the formation mechanism must be different from "normal star-forming" in which a bipolar outflow is produced by the collimation of the proto-stellar wind by the circumstellar disk. If they are jets produced by bullets with a speed comparable to the H_2 line width of $40-100$ km/s (Nadeau & Geballe 1979), tracks such as we observe could be produced in ~ 500 years. This compares with the estimate of 1000 years by Allen & Burton (1993) for the age of their jets, which are located further outside of OMC–1, to the north–west. At least in the case of the shorter and more numerous jets, it seems difficult to generate them solely with "bullets" from one or several central sources. The bright linear structures look rather similar, have similar lengths and therefore presumably also not very divergent ages. If the "bullets" were to be produced by numerous stellar sources they would have to have passed through the same ejection phase almost simultaneously in order to produce the morphology now observed. If, on the other hand, one single object emitted the "bullets", the precession rate would have to be extremely large, which in turn, would lead to warped jets which however are not observed.

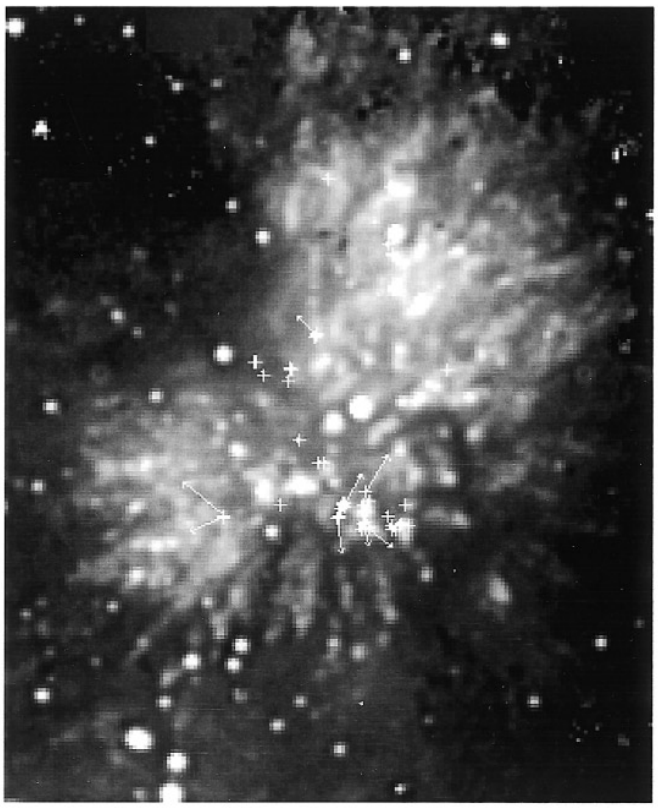

Fig. 11. H_2O maser positions and movements superposed on an image of molecular hydrogen taken at 2.12 μ.

6.1.2. The wind instability scenario

We find a rather smooth temperature distribution for OMC–1 which only varies radially and not as a function of position angle. Also kinematic observations of the S(1) 1–0 line profiles indicate that we see a spherically expanding shell with a velocity of a few ten kilometers per second (Scoville et al. 1982). This is more indicative of an uncollimated stellar wind which could be produced by a compact group of young massive stars in the IRc2 area. The collision of this wind with the surrounding dense material creates two shocked layers: The outer one consists of matter from the surrounding material and the inner one of the shocked wind (Pikel'ner 1968, Pikel'ner & Shcheglov 1969). Under various conditions instabilities can occur in the shell of

swept up material and it will fragment (e.g. Silk 1983). Recently, Stone et al. (1995) proposed a model where an early stellar wind coupled with gravitational deceleration produces a thin shell of material. This material is then shocked by a second, faster wind. In this situation, Rayleigh-Taylor instabilities will develop which may produce a morphology similar to the one observed in OMC–1.

Alternatively, instabilities also occur in a non-variable wind if the shocked envelope material is rapidly cooled. In this case, a thin layer develops which is highly unstable and which might quickly generate radial extensions which morphologically look very similar to jets. This "thin layer instability" has been studied in other astrophysical contexts (Dgani et al. 1993) but we suggest that it is also likely to play a role in the environment of OMC–1.

6.2. Coincidence of H_2O maser sources

A number of H_2O masers have been found in OMC–1 which, unlike masers from other molecules, are widely scattered over the outflow region. Those masers further away from the central area are also distinct because of their large proper motions (Genzel et al. 1981). In Fig. 11 we have drawn maser positions and directions of movement onto a 2.12 μm image. Interestingly, some of the fast moving masers are found close to the inner edge of H_2 fingers, with their velocity vectors pointing outwards into the same direction as the fingers.

Water masers in star forming regions are thought to be produced by a clumpy outflow from one or several young stellar sources. The maser lifetime is only a few years whereas the H_2 fingers must have ages of a few hundred years. It is therefore unlikely that there exists a generic link between H_2O masers and the H_2 linear structures unless the masers can be rejuvenated. The coincidence shown in Fig. 11 however indicates that both phenomena are linked and perhaps driven by the same mechanism.

6.3. Chemical evolution

The picture of OMC–1 where several supersonic flows interact with the surrounding molecular material could have important consequences for chemical models of this region. About a decade ago it was considered that warm ($T \sim 100$ K) cloud chemistry could account for what was observed (Herbst & Leung 1986). But more recent work by Herbst & Millar (1991) has stressed the need for the detailed physical conditions in dense clouds to be taken into account.

Reviewing chemical modeling of the region close to IRc2, they commented that existing models are based on a gross oversimplification of the physical conditions present in dense interstellar clouds. Our images indicate that explanations of the observed molecular abundances may have to be refined still further by taking into account the effect of narrow, highly collimated structures, giving rise to steep density gradients throughout the gas in which the resulting chemistry occurs.

Acknowledgements. It is a pleasure to thank the ESO infrared support group at La Silla for their dedicated help and the staff at UKIRT for their assistance. We are particularly indebted to Tom Geballe and John Davies for their spectroscopic service observations. We have benefitted from very fruitful discussions with Steve Shore and Rolf Walder and thank Thomas Dumm for his assistance in relation to the Fabry–Pérot transmission. HS acknowledges the financial support of the Swiss National Foundation. The UK Particle Physics and Astronomy Research Council are thanked for financial support to SM and JT.

References

Allen D.A, Burton M.G., 1993, Nature 363, 54
Bachiller R., Cernicharo J., 1990, A&A 239, 276
Bachiller R., Cernicharo J., Martín–Pintado J., Tafalla M., Lazareff B., 1990, A&A 231, 174
Bachiller R., Martín–Pintado J., Planesas P., 1991, A&A 251, 639
Beckwith S., Persson S.E., Neugebauer G., Becklin E.E., 1978, ApJ 223, 464
Black J.H., Van Dishoeck E.F., Willner S.P., Woods R.C., 1990, ApJ 358, 459
Chui, C.H., 1992, "An introduction to Wavelets", Wavelet analysis and its applications, Academic Press, Boston
Dalgarno A., 1994, Adv. At. Mol. Opt. Phys. 32, 57
Dgani R., Walder R., Nussbaumer H., 1993, A&A 267, 155
Dinelli B.M., Miller S., Tennyson J., 1992, J. Molec. Spectrosc. 153, 718
Drossart P., Maillard J.-P., Caldwell J., Kim S.J., Watson J.K.G., Majewski W.A., Tennyson J., Miller S., Atreya S., Clarke J., Waite J.H. Jr, Wagener R., 1989, Nature 340, 539
Gautier T.N., Fink U., Treffers R.R., Larson H.P., 1976, ApJ 207, L129
Geballe T.R., Oka T., 1989, ApJ 342, 855
Geballe T.R., Jagod M.-F., Oka T., 1993, ApJ 408, L109
Genzel R., Stutzki J., 1989 ARA&A 27, 41
Genzel R., Reid M.J., Moran M., Downes D., 1981, ApJ 244, 884
Guilloteau S., Bachiller R., Fuente A., Lucas R., 1992, A&A 265, L49
Herbst E., Leung C.M., 1986, MNRAS 222, 689
Herbst E., Millar T.J., 1991, in *Molecular Clouds* (Eds. James R.A. & Millar T.J., Cambridge University Press, Cambridge), 209
Irwin A.W., 1987, A&A 182, 348
Kao L., Oka T., Miller S., Tennyson J., 1991, ApJS 77, 317
Lane A.P., 1989, in "Low Mass Star Formation and Pre–Main Sequence Objects", ESO Conference and Workshop Proceedings No 33, p. 331
Lonsdale C.J., Becklin E.E., Lee T.J., Stewart J.M, 1982, AJ 87, 1819
Lucy L.B., 1974, AJ 79, 745
Mac Low M.–M., 1995, Nature 377, 287
Mallat S., 1989, Proc. IEEE Trans. on Pattern Anal. and Math. Intel., Vol. 11, No. 7
Mandy M.E., Martin P.G., 1993, ApJS 86, 199
McCaughrean M.J., Stauffer J.R., 1994, AJ 108, 1382
Menten K.M., Reid M.J., 1995, ApJ 445, L157
Meyer Y., 1992, "Les ondelettes", Algorithmes et Applications, A. Colin, Paris
Miller S., Tennyson J., Lepp S., Dalgarno A., 1992, Nature 355, 420
Mundt R., 1985, in Protostars and Planets II, Eds. Black D.C & Matthews M.S., University of Arizona Press, 414
Nadeau D., Geballe T.R., 1979, ApJ 230, L169
Neufield D.A., Dalgarno A., 1989, ApJ 340, 869

O'Dell C.R., 1995, in "Circumstellar disks, outflows and star formation", Revista Mexicana de Astronomia y astrofísica, Serie de conferencias Vol. 1, 11
Oka T., 1981, Phil. Trans. R. Soc. Lond. A, 303, 543
Pikel'ner S.B., 1968, Astrophys. Letters 2, 97
Pikel'ner S.B., Shcheglov P.V., 1969, SvA 12, 757
Ridgway S.T., 1983, in "Birth and Infancy of Stars", Les Houches, (Eds. R. Lucas, A. Omont, R. Stora), 507
Roberge W., Dalgarno A., 1982, ApJ 255, 176
Ròżyczka M., Tenorio-Tagle G., 1985, A&A 147, 202
Ruskai M.B., Beylkin G., Coifman R., Daubechies I., Mallat S., Meyer Y., Raphael L., 1992, "Wavelets and their Applications", Jones and Bartlett Publishers, Boston
Schild H., Miller S., Tennyson J., 1995, ESO Messenger No. 79, 24
Scoville N.Z., Hall D.N.B., Kleinmann S.G., Ridgway S.T, 1982, ApJ 253, 136
Silk J., 1983, in "Birth and Infancy of Stars", Les Houches, (Eds. R. Lucas, A. Omont, R. Stora), 349
Stone J.M., Xu J., Mundy L.G, 1995, Nature 377, 315
Sugai H., Usuda T., Kataza H., Tanaka M., Inoue M.Y., Kawabata H., Takami H., Aoki T., Hiromoto N., 1994, ApJ 420, 746
Trafton L.M., Geballe T.R., Miller S., Tennyson J., Ballester G.E., 1993, ApJ 405, 761

This article was processed by the author using Springer-Verlag LaTeX A&A style file *L-AA* version 3.